

LEVEL II

B.S. 12

AD A 072601



LASER IRRADIANCE IN THE SEA: THEORY AND EXPERIMENT

Lloyd C. Bobb
Gerald Ferguson
Michael Rankin

Sensors and Avionics Technology Directorate
NAVAL AIR DEVELOPMENT CENTER
Warminster, PA 18974

SEPTEMBER 1978

DDC FILE COPY

*Technical Research Report
NAVAIRDEVCEN Independent Research/
Exploratory Development Program
Approved for Public Release:
Distribution Unlimited; Report Issue Date 31 October 1978*

Prepared for
NAVAL AIR DEVELOPMENT CENTER
Department of the Navy
Warminster, Pennsylvania 18974

DDC
RECEIVED
AUG 13 1979
D

79 08 9 014

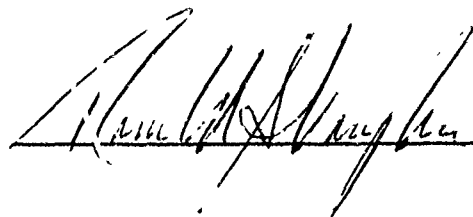
NOTICES

REPORT NUMBERING SYSTEM - The numbering of technical project reports issued by the Naval Air Development Center is arranged for specific identification purposes. Each number consists of the Center acronym, the calendar year in which the number was assigned, the sequence number of the report within the specific calendar year, and the official 2-digit correspondence code of the Command Office or the Functional Directorate responsible for the report. For example: Report No. NADC-78015-20 indicates the fifteenth Center report for the year 1978, and prepared by the Systems Directorate. The numerical codes are as follows:

CODE	OFFICE OR DIRECTORATE
00	Commander, Naval Air Development Center
01	Technical Director, Naval Air Development Center
02	Comptroller
10	Directorate Command Projects
20	Systems Directorate
30	Sensors & Avionics Technology Directorate
40	Communication & Navigation Technology Directorate
50	Software Computer Directorate
60	Aircraft & Crew Systems Technology Directorate
70	Planning Assessment Resources
80	Engineering Support Group

PRODUCT ENDORSEMENT - The discussion or instructions concerning commercial products herein do not constitute an endorsement by the Government nor do they convey or imply the license or right to use such products.

APPROVED BY:



DATE: _____

UNCLASSIFIED

SECURITY CLASSIFICATION OF THIS PAGE (When Data Entered)

REPORT DOCUMENTATION PAGE		READ INSTRUCTIONS BEFORE COMPLETING FORM	
1. REPORT NUMBER Technical Report NADC-78253-30		3. RECIPIENT'S CATALOG NUMBER	
4. TITLE (and Subtitle) Laser Irradiance in the Sea: Theory and Experiment		5. TYPE OF REPORT & PERIOD COVERED Technical Research Report	
7. AUTHOR(s) Lloyd C. Bobb Gerald Ferguson Michael Rankin		8. CONTRACT OR GRANT NUMBER(s) ZR00001	
9. PERFORMING ORGANIZATION NAME AND ADDRESS Naval Air Development Center Code 3012 Warminster, PA 18974		10. PROGRAM ELEMENT, PROJECT, TASK AREA & WORK UNIT NUMBERS 61152N, ZR00001, ZR01107 GC181	
11. CONTROLLING OFFICE NAME AND ADDRESS Naval Air Development Center Code 01 Warminster, PA 18974		12. REPORT DATE September 1978	
14. MONITORING AGENCY NAME & ADDRESS (if different from Controlling Office) 44p		13. NUMBER OF PAGES 42	
		15. SECURITY CLASS. (of this report) UNCLASSIFIED	
16. DISTRIBUTION STATEMENT (of this Report) Approved for Public Release; Distribution Unlimited			
17. DISTRIBUTION STATEMENT (of the abstract entered in Block 20, if different from Report)			
18. SUPPLEMENTARY NOTES 79 08 9 014			
19. KEY WORDS (Continue on reverse side if necessary and identify by block number) Laser Irradiance Beam Spreading Refraction Capillary Wave Heights Volume Scattering Capillary Wave Slopes Beam Steering Capillary Wave Spectrum			
20. ABSTRACT (Continue on reverse side if necessary and identify by block number) Laser beam spreading due to the air/sea interface, volume scattering, and initial beam divergence is modeled. Beam steering is considered for the case in which the laser beam diameter is small compared to the length of the refracting wave. An expression is developed for the irradiance as a function of depth into the ocean. A comparison of the terms in this expression shows that the surface			

DD FORM 1 JAN 73 1473

EDITION OF 1 NOV 65 IS OBSOLETE
S/N 0102-LF-014-6601

UNCLASSIFIED

SECURITY CLASSIFICATION OF THIS PAGE (When Data Entered)

UNCLASSIFIED

SECURITY CLASSIFICATION OF THIS PAGE (When Data Entered)

spreading effect is small compared with bulk scattering. Wavetank experiments were performed. The height, slope, and frequency content of wind-driven capillary waves are reported for wind speeds in the range 2.2 m/sec to 7.6 m/sec.

Accession For	
NTIS GRA&I	<input checked="checked" type="checkbox"/>
DDC TAB	<input type="checkbox"/>
Unannounced	<input type="checkbox"/>
Justification	
By	
Distribution/	
Availability Codes	
Avail and/or special	
A	

UNCLASSIFIED

SECURITY CLASSIFICATION OF THIS PAGE (When Data Entered)

NADC-78253-30

ACKNOWLEDGEMENTS

The authors wish to acknowledge the help of Mr. Gwyn Woodward, Mr. Robert Starry, and Mr. Howard Krumboltz on the experimental portions of this paper. Additionally, the authors are grateful to Dr. Patrick Manzo for the irradiance calculation.

TABLE OF CONTENTS

<u>Section</u>		<u>Page</u>
	EXECUTIVE SUMMARY	S-1
1	INTRODUCTION	1-1
2	SMALL BEAM CASE	2-1
3	LARGE BEAM CASE	3-1
4	BULK SCATTERING	4-1
5	EXPERIMENTAL APPARATUS	5-1
6	EXPERIMENTAL RESULTS	6-1
7	CCNCLUSIONS	7-1
	REFERENCES	R-1

LIST OF ILLUSTRATIONS

<u>Figure</u>		<u>Page</u>
1	Theoretical Velocity and Frequency Curves for Waves on Water	1-3
2	Beam Deflection Geometry	2-2
3	Beam Spread Versus Wind Speed	3-3
4	Small Angle Scattering Approximation	4-2
5	Beam Radius Versus Depth	4-5
6	Wavetank Apparatus	5-2
7	Wave Height Distribution for a 5.8 m/sec Wind Speed . . .	6-3
8	Wave Height Versus Wind Speed	6-3
9	Wave Spectral Content at Specific Wind Speeds	6-4
10	Wave Slope Distribution for $W = 2.2$ m/sec	6-6
11	Wave Slope Distribution for $W = 3.1$ m/sec	6-6
12	Wave Slope Distribution for $W = 4.0$ m/sec	6-6
13	Wave Slope Distribution for $W = 4.9$ m/sec	6-6
14	Wave Slope Distribution for $W = 5.8$ m/sec	6-7
15	Wave Slope Distribution for $W = 6.7$ m/sec	6-7
16	Wave Slope Distribution for $W = 7.6$ m/sec	6-7
17	RMS Wave Slope Versus Wind Speed	6-9
18	Beam Divergence Versus Wind Speed	6-10
19	Capillary Wave Forms	6-12

NADC-78253-30

LIST OF TABLES

<u>Table</u>		<u>Page</u>
1	Integrated Probability Versus Δ/σ_0	2-3
2	Beam Deflection Versus Wind Speed	2-3
3	Wind-Driven Wave Heights	6-1

EXECUTIVE SUMMARY

INTRODUCTION

The Adaptive Optics task was funded under the IR Program. The purpose of the study was twofold:

- a. Determine the importance of the air/sea interface in the degradation of laser beam irradiance
- b. Examine the possibility of using adaptive optical techniques to compensate for the interface

BACKGROUND

When a laser beam is directed from an airborne platform to a target under the water, the irradiance is diminished by the initial beam divergence, atmospheric scattering and absorption, the air/sea interface, and bulk scattering in the ocean. By using the small angle scattering approximation of electron scattering theory and a modified Cox and Munk probability distribution for sea slopes, an expression is derived which predicts the laser beam radius as a function of distance (z) into the water. A comparison of the terms in the resultant expression for beam radius shows that the bulk scattering term dominates over the surface spreading term for $z > 10$ meters in very good water ($s \sim .05\text{m}^{-1}$) and high wind speeds ($\sim 10\text{m/s}$).

It was decided to make a careful determination of the capillary wave slope distribution in the laboratory because the Cox and Munk values are smaller than the theoretical values. Additionally, if the slope distribution was determined to be much larger, then the conclusion about the relative importance of the interface would be changed accordingly.

CONCLUSIONS

The following conclusions can be drawn from this study:

- a. The beam spreading due to the roughness of the air-sea interface is small compared with the spreading due to bulk scattering. Therefore, compensating for the interface would be of little benefit.

- b. Using a small-diameter laser beam substantially increases the irradiance on target for depths of 50 meters and less.
- c. The mean heights for capillary waves are in the range 0.06 to 8.8 millimeters for wind speeds 2.2 to 7.6 meters per second. These heights are consistent with theoretically allowed values for capillary waves.
- d. The spectral content of the wind-driven capillary waves is in the range 0 to 400 Hz with most of the intensity below 100 Hz. The high-frequency portions of the spectral curves grow at the expense of the low-frequency portions as the wind speed increases.
- e. The wavetank data on wave slopes yield higher values for full-width beam divergence (~5 degrees) than open-ocean data (~2 degrees and ~4 degrees) at wind speeds in the range of 5 to 8 meters per second.
- f. Fewer wave slopes of high angle are measured in these experiments than are predicted by theory.
- g. The onset wind velocity for wave generation is found to be ~3 meters per second.
- h. The shape of the wind-driven waves is affected by the wind.
- i. The wave height measurements furnish experimental support to the theoretical model of Crapper.

RECOMMENDATIONS

- 1. It is not worthwhile pursuing adaptive optical methods to compensate for ocean roughness.
- 2. For the purposes of air-to-underwater communication, bathymetry, and designation, higher rms wave slopes can be used than those given by Cox and Munk.

SECTION 1
INTRODUCTION

This study was initiated to establish the feasibility of using adaptive optic techniques to compensate for the distortion of light (laser) beams caused by traversing the air-sea interface. Before designing a specific system which could sense the ocean surface waveforms and tailor the laser beam wave front to compensate for the interface, it was decided to model the interface, the volume scattering, and the incident beam characteristics to establish the relative effect of the interface.

Several wavetank experiments on wind-driven capillary waves were planned and performed. The purpose of these experiments was to measure the capillary wave heights, slopes, and frequencies. These physical parameters are important to the adaptive optics approach.

The hydrodynamics of waves in water has been worked out by various authors. A particularly readable approach has been published by Clark (Reference 1). A result of this calculation is that the speed (U) of propagation for a gravity wave is:

$$U = \frac{\omega}{k} = \left[\left(\frac{g}{k} \right) \tanh kz \right]^{1/2} \quad (1)$$

where:

ω = the frequency,

k = the wave vector $\left(\frac{2\pi}{\lambda} \right)$,

g = the gravitational constant, and

z = the depth.

Where $\lambda \ll z$, equation (1) becomes

$$U \approx \left(\frac{g}{k} \right)^{1/2} \quad (2)$$

In accordance with equation (2), the velocity of gravity waves increases as $\lambda^{1/2}$ power. Stokes (Reference 2) showed that the maximum height, trough to crest, for gravity waves is 0.14 wavelengths. If the surface tension (S) is included in the calculation for wave velocity, we find that:

$$U = \left[\left(\frac{g}{k} \right) + \left(\frac{S k}{\rho} \right) \right]^{1/2} (\tanh kz)^{1/2} \quad (3)$$

where ρ is the density. Again, where $\lambda \ll z$, equation (3) becomes:

$$U = \frac{\omega}{k} \approx \left[\left(\frac{g}{k} \right) + \left(\frac{S k}{\rho} \right) \right]^{1/2} \quad (4)$$

A plot of equation (4) is shown in Figure 1. From the curves in Figure 1, it can be seen that the minimum velocity for capillary waves is approximately 23 cm/sec; the minimum frequency is about 13 Hz; and the maximum wavelength is 1.7 cm. Also, it is seen that the wave velocity increases as the capillary wavelength decreases (anomalous dispersion) in contrast to the gravity wave velocity. One additional feature of the frequency curve shown in Figure 1 is the rapid increase in frequency with a decrease in the capillary wavelength. In a theoretical paper by Crapper (Reference 3), it is shown that the wave of greatest height occurs when the trough to crest distance is 0.73λ . This number is approximately five times greater than the comparable one for gravity waves. It is also shown in this paper that the velocity of capillary waves is moderately diminished at higher amplitudes (the factor being 0.8 for $\frac{a}{\lambda} = 0.73$).

The slope of a wave at any point is important to this study because of the relationship between slope angle and beam deflection. The change of slope over the laser beam area causes the beam to spread. Therefore, it is essential to

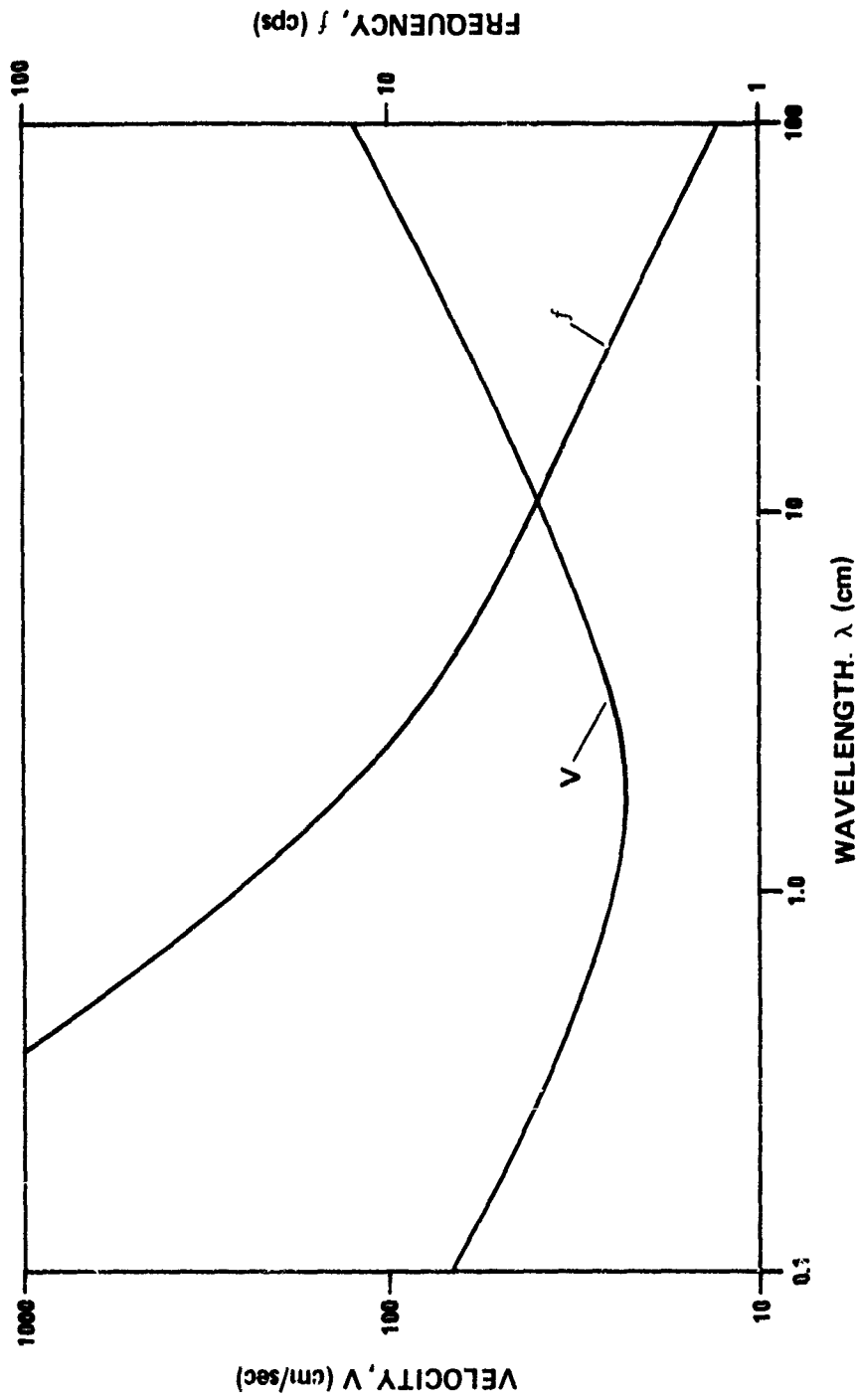


Figure 1. Theoretical Velocity and Frequency Curves for Waves on Water

understand wave slope statistics. Of the many studies on wave slope statistics in the open ocean, the Cox and Munk study (Reference 4) is the most comprehensive. One of the results of the Cox and Munk study is that the wave slopes may be described by a Gram Charlier distribution. This distribution is the product of a two-dimensional Gaussian distribution and an infinite series of Hermite polynomials. To a very good approximation, the Gram Charlier distribution may be replaced by a Gaussian distribution as follows:

$$P(\sigma) = \frac{1}{2\pi \sigma_c \sigma_u} \exp - \left[\frac{\sigma^2}{4} \left(\frac{1}{\sigma_u^2} + \frac{1}{\sigma_c^2} \right) \right] . \quad (5)$$

The mean square slope components are σ_u^2 and σ_c^2 , the upwind and crosswind, respectively. Cox and Munk measured these slopes to be:

$$\sigma_c^2 = 0.003 + 1.92 \times 10^{-3} W \pm 0.002 \quad (6)$$

and

$$\sigma_u^2 = 0.000 + 3.16 \times 10^{-3} W \pm 0.004 \quad (7)$$

where W is the wind speed in meters per second (m/sec). For the one-dimensional case, equation (5) can be reduced to:

$$P(\sigma) = \frac{1}{\sqrt{\pi} \sigma_o} \exp - \left(\frac{\sigma}{\sigma_o} \right)^2 \quad (8)$$

where $\sigma_o = \sigma_u$. The probability distribution in equation (8) is normalized to one (1); that is,

$$\int_{\sigma} P(\sigma) d\sigma = 1 . \quad (9)$$

Two features of the above distribution are that it is very narrow at low wind speeds, and the average wave slope is zero. Neither feature is exactly true, but they are reasonable approximations. The wave slope distribution can now be used in the calculation for beam steering and beam spreading.

SECTION 2

SMALL BEAM CASE

Consider a laser beam, small in diameter compared to the length of the refracting ocean wave, incident on a wave of slope σ . As depicted in Figure 2, the transmitted beam has deviated from its original direction by an amount Δ . The relationship between σ and Δ is determined by Snell's Law as follows:

$$n \sin \sigma = n' \sin \theta' \quad (10)$$

and, in the small angle approximation,

$$n \sigma \approx n' \theta'. \quad (11)$$

From Figure 2,

$$\Delta = \sigma - \theta' \approx \sigma - \left(\frac{n}{n'}\right) \sigma \quad (12)$$

or

$$\Delta \approx \sigma \left(1 - \frac{n}{n'}\right). \quad (13)$$

For the case of seawater,

$$\Delta \approx \frac{\sigma}{4}. \quad (14)$$

From equation (14) it can be seen that the beam deflection (Δ) is approximately one-fourth of the wave slope (σ). This result will be used in the one-dimensional wave slope distribution, equation (8), to determine beam deflection probability.

Substituting equation (14) into equation (8) and normalizing, we find that:

$$P(\Delta) = \frac{4}{\sqrt{\pi} \sigma_0} \exp - 16 \left(\frac{\Delta}{\sigma_0}\right)^2. \quad (15)$$

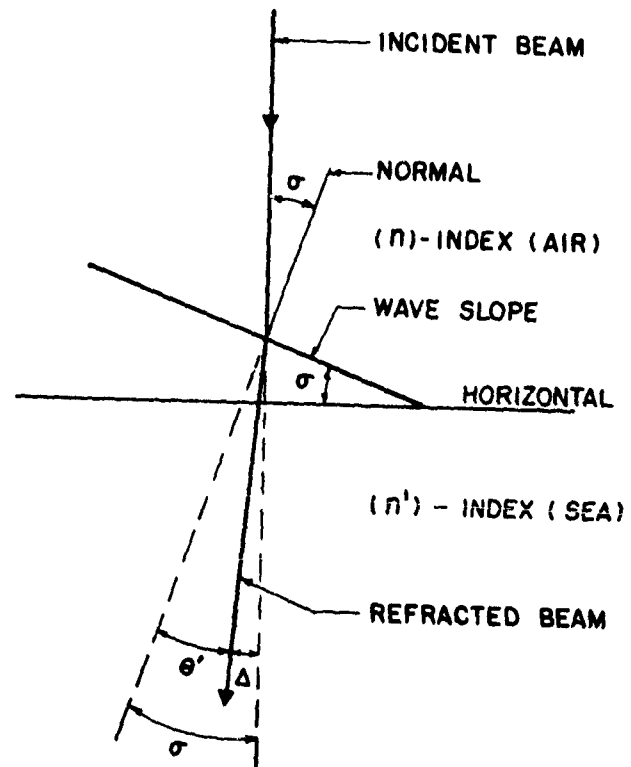


Figure 2. Beam Deflection Geometry

Equation (15) shows the probability that the beam is deflected by an amount Δ . In order to determine the angular limits that contain the beam for a given percentage of the time, equation (15) is integrated. The results of this integration are given in Table 1. The significance of the results in Table 1 is that the beam deflection is related to the root mean square (rms) wave slope σ_0 by a probability. For example, the probability is 0.8 that $\Delta \leq 0.23 \sigma_0$, and the probability is 0.5 that $\Delta \leq 0.12 \sigma_0$. For this calculation, Δ is the half-angle value. The results of calculating the probability that the beam deflection is within defined angular limits at a given wind speed are listed in Table 2. For example, for a 4-meter-per-second wind speed, the probability is 0.50 that the beam is deflected within 13 milliradians and 0.80 that the beam is deflected within 26 milliradians. The results in Table 2 for the small beam case will be compared with the beam-spreading results for the large beam case.

TABLE 1. INTEGRATED PROBABILITY VERSUS Δ/σ_0

INTEGRATED PROBABILITY	0	0.2	0.4	0.5	0.6	0.7	0.8	0.9	0.96
Δ/σ_0	0	0.046	0.094	0.12	0.15	0.184	0.23	0.29	0.36

TABLE 2. BEAM DEFLECTION VERSUS WIND SPEED

WIND SPEED (m/sec)	σ_0 (radians)	Δ (P = 0.5) (radians)	Δ (P = 0.8) (radians)
4	0.11	0.013	0.026
8	0.16	0.019	0.037
12	0.19	0.023	0.045

SECTION 3

LARGE BEAM CASE

For the case in which the diameter of the laser beam is large compared with the ocean wavelength encountered, the beam is spread by the air/sea interface as opposed to being deflected. The large beam case is the integral of the small beam case over the beam diameter. We assume that the input beam $f_o(\theta, r)$ is distributed in the following manner:

$$f_o(\theta, r) = \frac{1}{\pi \theta_o R_o} \exp - \left[\left(\frac{\theta}{\theta_o} \right)^2 + \left(\frac{r}{R_o} \right)^2 \right] \quad (16)$$

where

R_o = the radius at which the beam decays to $\frac{1}{e}$ times its value at $r = 0$
and

θ_o = the angle at which the beam decays to $\frac{1}{e}$ times its value at $\theta = 0$.

The output beam distribution function $f_1(\theta', r)$, which describes how the beam is distributed under the sea surface, is obtained by integrating the product of the input beam distribution function and a modified probability distribution for sea slopes over all input angles, as follows:

$$f_1(\theta', r) = \int f_o(\theta, r) P(\theta', \theta) d\theta. \quad (17)$$

In equation (17), θ and θ' are measured from the vertical, and $P(\theta', \theta)$ is the probability of obtaining θ' under the surface for an input angle of θ . The result of this integration is:

$$f_1(\theta', r) = \frac{1}{\pi R_o \Theta} \exp - \left[\left(\frac{r}{R_o} \right)^2 + \left(\frac{\theta'}{\Theta} \right)^2 \right] \quad (18)$$

where:

$$\Theta = \frac{\left[\sigma_o^2 (\beta - 1)^2 + \theta_o^2 \right]^{1/2}}{\beta}. \quad (19)$$

In equation (19), $\beta = \frac{n'}{n}$. The output beam distribution function depends on the initial beam divergence and the sea state. Equation (19) is shown in graphical form in Figure 3. It can be seen in Figure 3 that there is very little difference between the $\theta_0 = 0.000$ radians curve and the $\theta_0 = 0.010$ radians curve for wind speeds greater than 2 meters per second. Most laser divergence cases would fall close to these two curves. Note that in Figure 3, for a low divergence laser beam (0.000 to 0.010 radians), the beam spreading will be 28 milliradians for a 4-meter-per-second wind speed and 40 milliradians for an 8-meter-per-second wind speed. These values are comparable to the values in Table 2 for the small beam case when the probability is 80 percent. The 80-percent probability case corresponds very closely to the output beam distribution function being multiplied by $\left(\frac{1}{e}\right)$; it is for this reason that we use the 80-percent probability case. This beam spreading result will be incorporated into an equation for the irradiance in the next section.

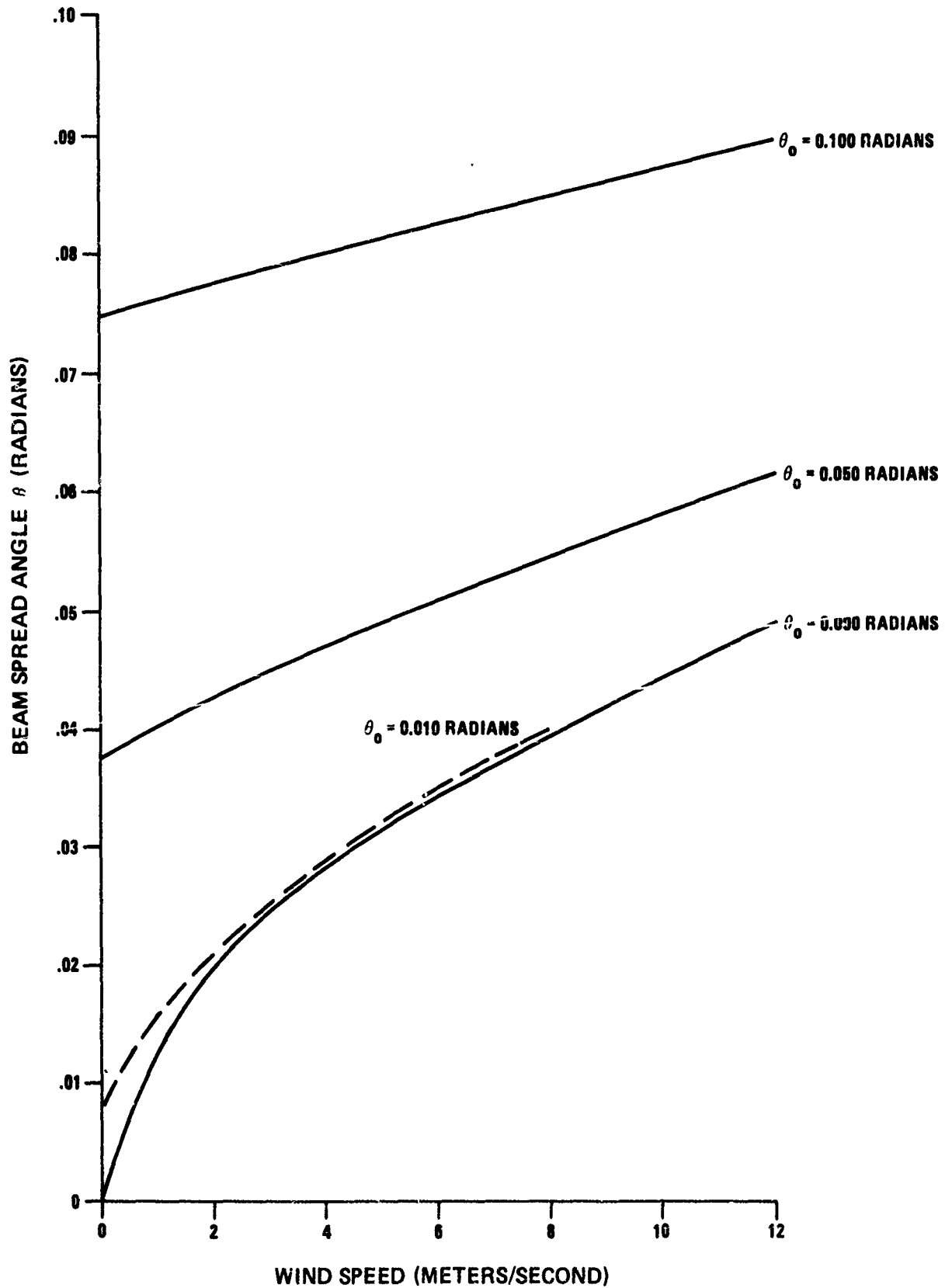


Figure 3. Beam Spread Versus Wind Speed

SECTION 4

BULK SCATTERING

In this section the approach of Arnush (Reference 5) is used to obtain an expression for the irradiance as a function of depth z . The small angle scattering approximation of electron scattering theory is used. The reasonably good fit at small angles to existing experimental data is shown in Figure 4. The normalized scattering function $\Sigma(\theta)$, which is defined as the volume scattering function divided by the scattering coefficient, is of the following form:

$$\Sigma(\theta) = \frac{\gamma \exp(-\gamma \theta)}{2 \pi \theta}, \quad \gamma \simeq 10. \quad (20)$$

The integral of the normalized scattering function is used in a formal expression for the irradiance. The result of this calculation is:

$$h(z, r, t) = \frac{g(t) e^{-az}}{\pi R_1^2} \exp\left(-\frac{r^2}{R_1^2}\right) \quad (21)$$

where:

$$R_1^2 = \frac{2 s z^3}{3 \gamma^2} + R_0^2 + z^2 \Theta^2. \quad (22)$$

In the above equations,

h = the scalar irradiance,

$g(t)$ = a time-dependent amplitude which depends on the source strength,

a = the volume absorption coefficient,

s = the volume scattering coefficient,

R_0 = the radius at the surface at which the beam decays to $\frac{1}{e}$ times the value at the center, and

Θ = the angular spread of the beam just below the surface.

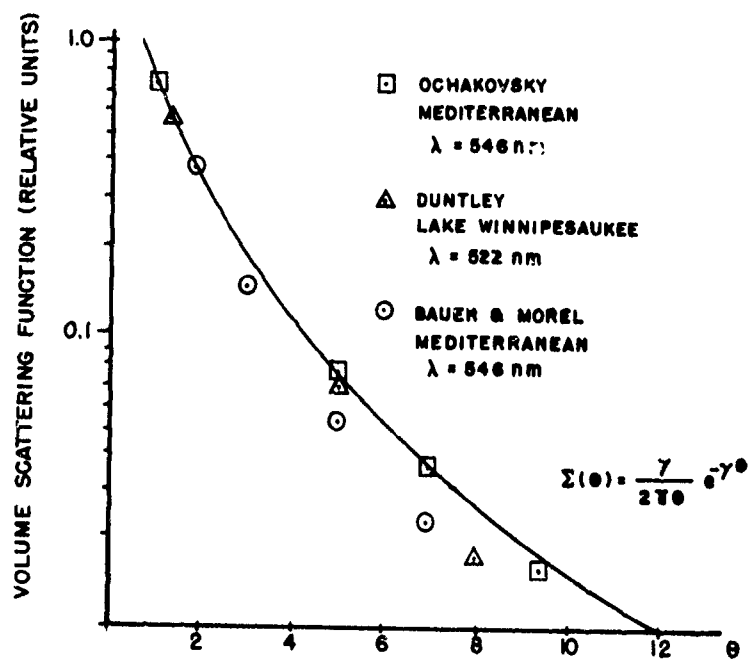


Figure 4. Small Angle Scattering Approximation

The amount of energy passing through an aperture of radius ρ centered on the beam is given by:

$$E(\rho, z, t) = 2\pi \int_0^\rho r \, dr \, h(z, r, t) \quad (23)$$

$$= g(t) e^{-az} \left(1 - e^{-\frac{\rho^2}{R_1^2}} \right) \quad (24)$$

In equation (24), one-half the energy passes through the aperture when:

$$\exp\left(-\frac{\rho^2}{R_1^2}\right) = 1/2 \quad (25)$$

or:

$$\rho_{1/2} = (0.693 R_1^2)^{1/2} = 0.833 (R_1^2)^{1/2} \quad (26)$$

And, finally,

$$\rho_{1/2} = 0.833 \left(\frac{2 s z^3}{3 \gamma^2} + R_o^2 + z^2 \theta^2 \right)^{1/2} \quad (27)$$

Equation (27) yields the functional relationship between the half-power radius ($\rho_{1/2}$) and the beam dissipation mechanisms. The first term in the parentheses shows the z^3 dependence due to bulk scattering. This term will clearly dominate at large depths. The second term is the surface spot size and dominates at small z values. The last term represents the surface spreading due to beam divergence and sea state.

By equating the spot size term and the spreading term in equation (27) to the bulk scattering term, the depth at which bulk scattering begins to dominate

can be calculated. The depth to which the beam radius term dominates over the scattering term is:

$$z_{R_0} = \left(\frac{3 \gamma^2 R_0^2}{2 s} \right)^{1/3} \quad (28)$$

For $\gamma = 10$, $R_0 = 10$ meters, and $s = 0.1 \text{ meters}^{-1}$, we find that $z_{R_0} \simeq 50$ meters. Therefore, the beam radius term dominates the scattering term to a depth of 50 meters for an initial beam radius of 10 meters. Clearly, the initial beam size is very important in determining the half-power radius.

A comparison of the bulk scattering term and the surface spreading term yields:

$$z_\theta = \frac{3 \gamma^2}{2 s} \theta^2 \quad (29)$$

where z_θ is the depth at which the bulk scattering term and the surface spreading term are equal. For a surface spreading term of 0.040 radians, $s = 0.05 \text{ meter}^{-1}$, and $\gamma \sim 10$, we find that $z_\theta \simeq 4.8$ meters. This is a very important result. The bulk scattering term dominates over the surface spreading term from 4.8 meters and deeper, even for very good water ($s = 0.05 \text{ meter}^{-1}$) and an 8-meter-per-second wind speed.

Various plots of equation (27) are shown in Figure 5 for a scattering coefficient of 0.1 meter^{-1} . The parameters used for R_0 and θ are not physically realistic but are presented for didactic reasons. The benefit of using a small beam for increasing the irradiance is readily apparent. It is also clear that there is very little benefit in correcting for the sea surface; at 50 meters the correction would result in only a 2-percent decrement in beam radius for the conditions given in Figure 5. The dominance of the bulk scattering term ($\rho \propto z^{3/2}$) at large depths is quite clear in Figure 5.

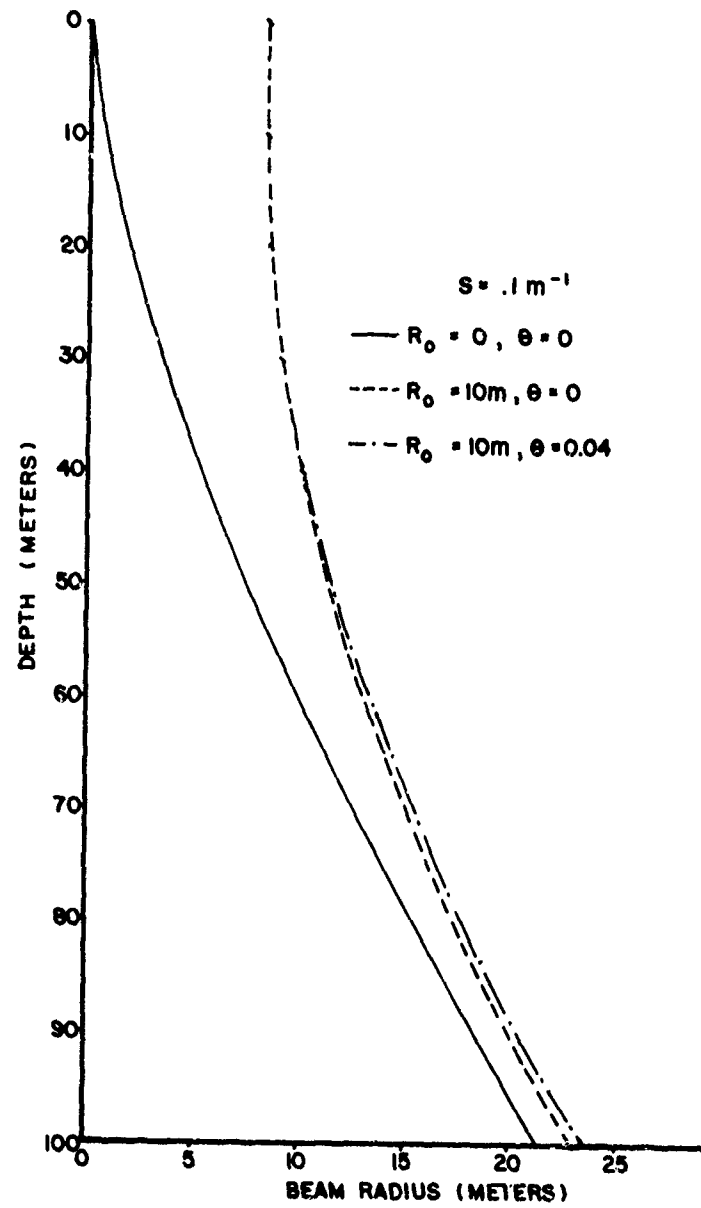


Figure 5. Beam Radius Versus Depth

SECTION 5

EXPERIMENTAL APPARATUS

The experimental studies were begun with the idea in mind that adaptive optic techniques might be utilized to compensate for the fine-scale roughness of the sea surface. It is the fine-scale roughness due to capillary waves that contributes markedly to beam spreading. Therefore, it was decided (1) to measure the capillary wave heights, as this defines the needed alteration of the wave front; (2) to measure the frequency content from which the length of the fine-scale roughness and the time constant of the surface state can be calculated; and (3) to measure the wave slope distribution, which determines the beam divergence under the surface.

The experimental apparatus for measuring wind-driven wave heights is shown in Figure 6. The wavetank is a rectangular box (28 cm width x 19 cm height x 117 cm length) fabricated from clear Plexiglas. Mounted in one end of the wavetank is a tangential blower driven by a variac. The blower forces air into an aluminum plenum which provides a laminar flow of air over the water surface for a length of 20 cm. The capillary waves are generated within this region of uniform air flow. The air velocity across the exit opening of the plenum varies less than 10 percent for the range of wind speeds used in these experiments (2.2 meters per second to 7.6 meters per second). The wind speeds were measured with a Pitot tube and an Alnor Velometer. At the end of the wavetank opposite to the blower is a sloping aluminum plate used to damp out the capillary waves. A Spectra Physics Model 155 He-Ne laser is mounted vertically above the wavetank and illuminates the water surface 10 centimeters from the end of the plenum. The laser beam diameter is 1 millimeter. The laser beam traverses the wavetank and enters the light collection system through a narrow slit. The slit size for the wave height measurements was 0.6 cm x 1.2 cm. A slit of this size eliminates the light which has traversed long paths

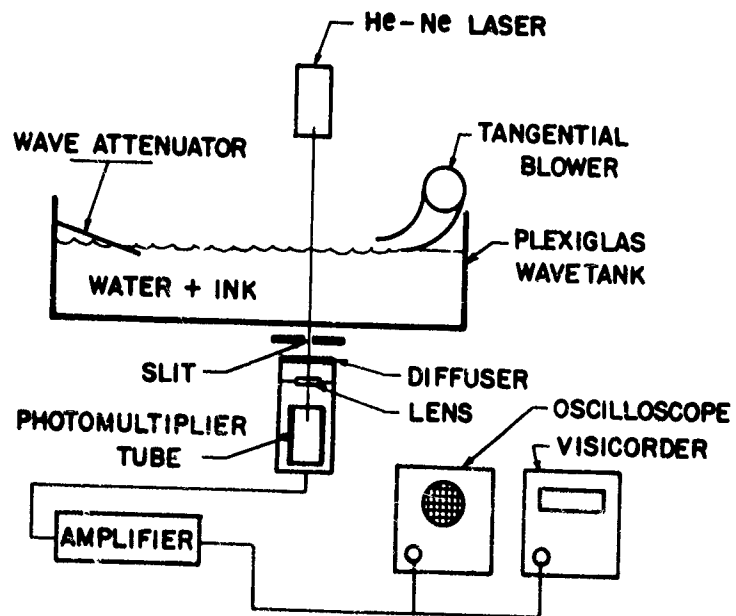


Figure 6. Wavetank Apparatus

through the water from being collected. The light collection system includes a diffusing screen and a collecting lens which uniformly illuminates the surface of an RCA 6199 photomultiplier tube. This system eliminates the problem associated with the photomultiplier tube output varying with the location of the illumination. The photomultiplier tube output is amplified and simultaneously displayed by a Tektronix Type 547 Oscilloscope and is recorded by a Honeywell Model 1508 Visicorder. The visicorder galvanometer has a 1 kHz response. The wavetank was filled to a depth of 8.5 centimeters with distilled water. The water was filtered to eliminate scattering from particulates. For the wave height measurements, ink was added to the water to yield a solution attenuation coefficient of $\alpha = 0.85 \text{ cm}^{-1}$. This coefficient was obtained by filling a 1-centimeter sample cell with the ink solution and measuring the attenuation of an He-Ne laser beam through the cell with an EG&G Radiometer.

The apparatus used to measure the wave spectrum is, to a large extent, the same as that in Figure 6. The differences are that clear water is used, the collection slit is narrowed to 0.2 cm x 1.2 cm, the amplifier is eliminated, and the visicorder is replaced by a Tektronix 3L5 Spectrum Analyzer in a Type 564 Storage Oscilloscope.

For the wave slope measurements the slit dimensions were 0.2 cm x 1.2 cm. The photomultiplier tube was translated in 0.2-centimeter increments parallel to the wind direction. The signal was averaged using an operational amplifier integrating circuit with a 10-second time constant. At least 2 minutes were allowed to elapse in each position to accumulate data before the voltage was read by a Hewlett Packard Model 400H vacuum tube voltmeter.

SECTION 6

EXPERIMENTAL RESULTS

Fluctuations in the laser intensity were recorded in real time by the visicorder. The wave height distribution was calculated at various wind speeds from variations in the laser beam intensity after traversing the wavetank. The governing equation is:

$$\frac{dI}{I} = -\alpha \delta \quad (30)$$

where:

dI = the incremental change in intensity I ,

α = the attenuation coefficient $0.85 \text{ centimeter}^{-1}$, and

δ = the trough to crest wave height.

Using the above attenuation coefficient, a 1-millimeter high wave yields an 8.5-percent change in signal, which is well above the noise. In fact, for the wave height experiments the high-frequency noise ($\sim 200 \text{ Hz}$), which averages out, is ~ 5 percent, and the low frequency noise ($\sim 10 \text{ Hz}$) is ~ 1 percent. This permits wave heights ~ 0.1 millimeter to be measured. In Table 3 the wave heights and the standard deviations are listed for various wind velocities. The standard

TABLE 3. WIND-DRIVEN WAVE HEIGHTS

WIND SPEED (meters/second)	WAVE HEIGHT (millimeters)
2.2	0.06 ± 0.15
3.1	0.32 ± 0.16
4.0	1.2 ± 0.7
4.9	1.5 ± 0.6
5.8	2.8 ± 0.9
6.7	3.9 ± 1.3
7.6	8.8 ± 3.6

deviations on the two lowest data points (2.2 m/sec and 3.1 m/sec) are a result of the system noise. The standard deviations on the rest of the data are a result of the wave heights being broadly distributed at each wind speed. The wave height distribution for a 5.8-meter-per-second wind speed is shown in Figure 7. The data in Figure 7 typify the results at other wind speeds. Therefore, each wind speed is not well-characterized by a single wave height. A plot of the data in Table 3 is shown in Figure 8. It can be seen in Figure 8 that the mean value of the wave height increases monotonically with wind speed from a value of $\bar{\delta} = 0.06$ mm at 2.2 meters per second to $\bar{\delta} = 8.8$ mm at 7.6 meters per second. Several features in Figure 8 are worth noting. The highest mean wave height ($\bar{\delta} = 8.8$ mm) is within the allowable height for capillary waves ($1.73 \text{ cm} \times 0.73 = 1.24 \text{ cm}$). The second feature is that capillary waves first appear at a wind speed of 2.2 meters per second. This value is slightly on the low side for our fetch (30 cm) if the data are compared with Cox's (Reference 6). Cox found that, for a 1.47-meter fetch, $U_0 = 2.9$ meters per second, where U_0 is the wind speed below which the mean square slope is extremely small. In the present study the extrapolation of the mean square slope to zero yields a higher value for the onset wind speed for capillary wave generation as will be seen subsequently.

The spectral intensity versus frequency curves for specific wind speeds are shown in Figure 9. It can be seen in these plots that the lower frequencies fall off in intensity with increasing wind speed, while the higher frequencies increase in intensity. Most of the spectral intensity occurs below 100 Hz ($\lambda > 0.35$ centimeter) even at the highest wind speeds measured in these experiments (7.6 meters per second). There are very few waves of a frequency greater than 300 Hz; this corresponds to wavelengths less than 0.17 centimeters. Therefore, in these experiments most of the measurements are on waves in the wavelength range of 0.35 centimeters to 1.7 centimeters and in the frequency range 100 Hz to 13 Hz.

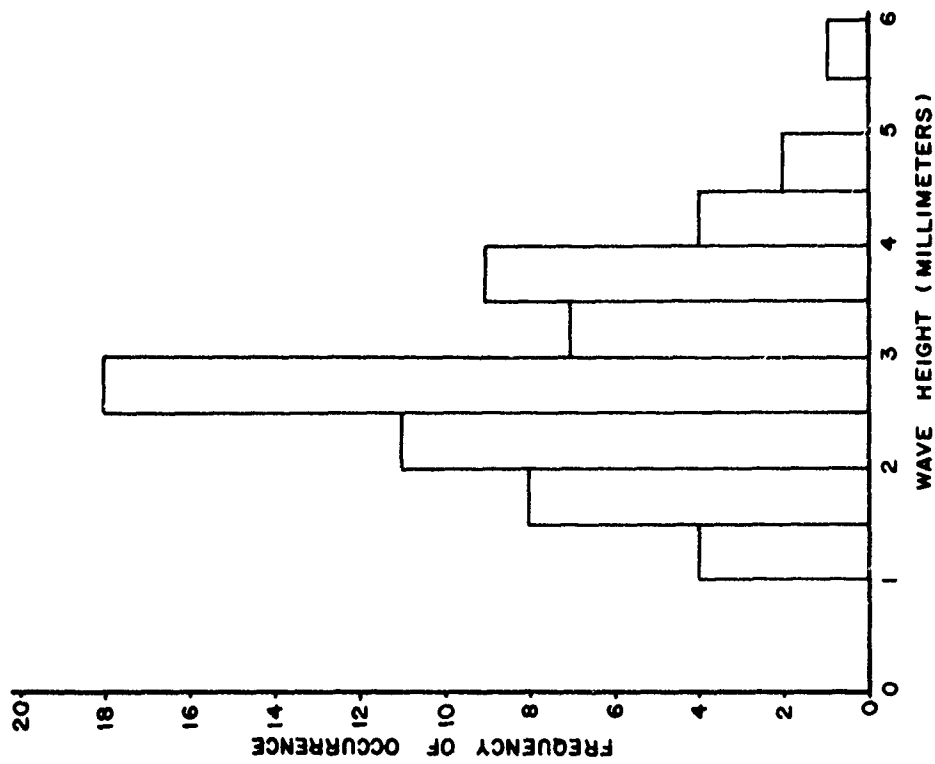


Figure 7. Wave Height Distribution for a 5.8 m/sec Wind Speed

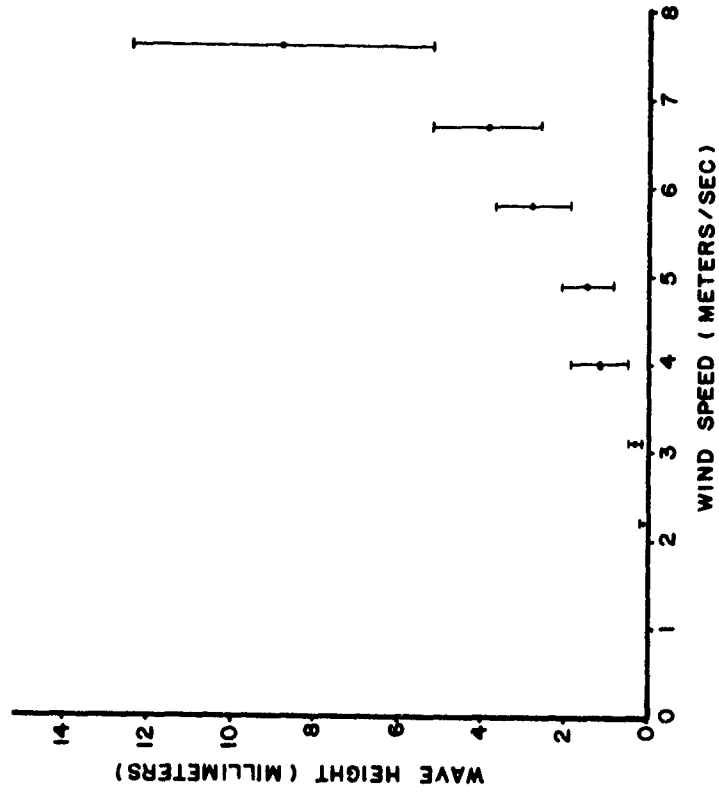


Figure 8. Wave Height Versus Wind Speed

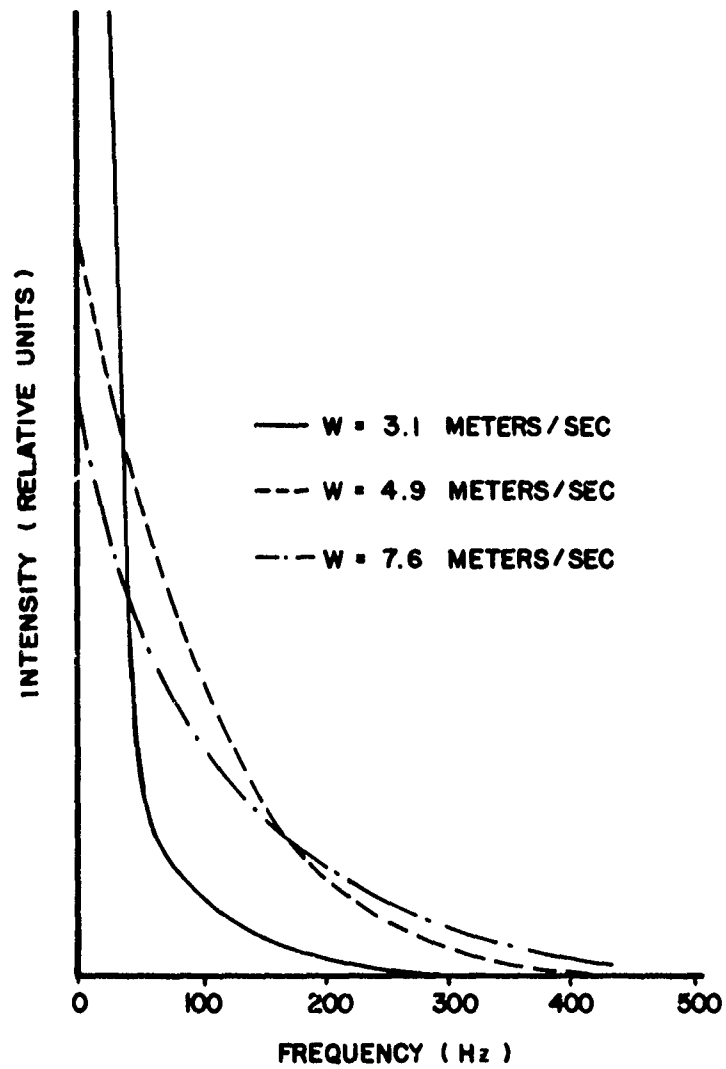


Figure 9. Wave Spectral Content at Specific Wind Speeds

In Figures 10 through 16, the wave slope distributions are shown at wind speeds in the range 2.2 meters per second to 7.6 meters per second. The data in each figure are corrected for photomultiplier tube dark noise and ambient illumination. In monitoring the pulse heights during the integration time, it was found that there was a systematic but small fall-off of signal level with angle; the data as shown are also corrected for this. The slit width (2 millimeters) corresponds to 1.22 degrees of collection angle which is equal to ~ 4.9 degrees of wave slope. The tube is translated in increments of 2 millimeters; therefore, there is no overlap in data collecting from one reading to the next.

In Figure 10 the histogram for the 2.2 meters per second wind speed is shown. There are waves present at this wind speed as indicated from the wave height measurements. However, all of the slopes present are within the central 4.9 degrees (± 2.45 degrees); therefore, no intensity is measured beyond this region. It would take a smaller slit to measure the slope distribution at this wind speed (2.2 meters per second). An additional feature of the data is that the areas under the histograms in Figures 10 through 16 are nearly constant. (Note the scale change in Figures 12 through 16.) The nearly constant areas result from the fact that nearly all of the refracted light is collected. Therefore, at higher wind speeds the central region diminishes as the intensity at higher angles grows. In looking at Figures 10 to 16 it is noticed that, for wind speeds equal to 4.9 meters per second and greater, the peak of the slope distribution is shifted towards the downwind direction. This same behavior was seen by Cox and Munk (Reference 4) and Prettyman and Cermak (Reference 7) in their ocean measurements. Besides this asymmetry in the data, it is seen that the intensities are different at high angles (greater than 30 degrees) for the windward and leeward sides of the waves. The shapes of the histograms show that the shape of the wind-driven waves is affected by the wind. On the windward side of the waves, the wave slope is in the low angle positions longer and in the high angle positions for a shorter time than on the leeward side of the waves.

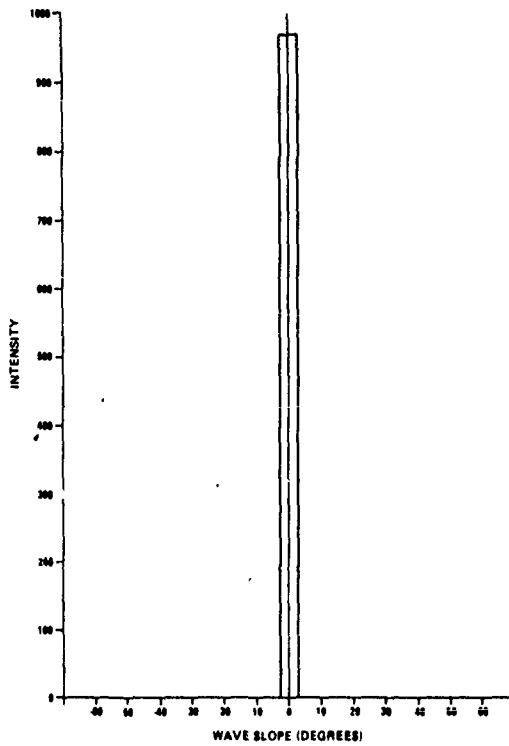


Figure 10. Wave Slope Distribution
for $W = 2.2$ m/sec

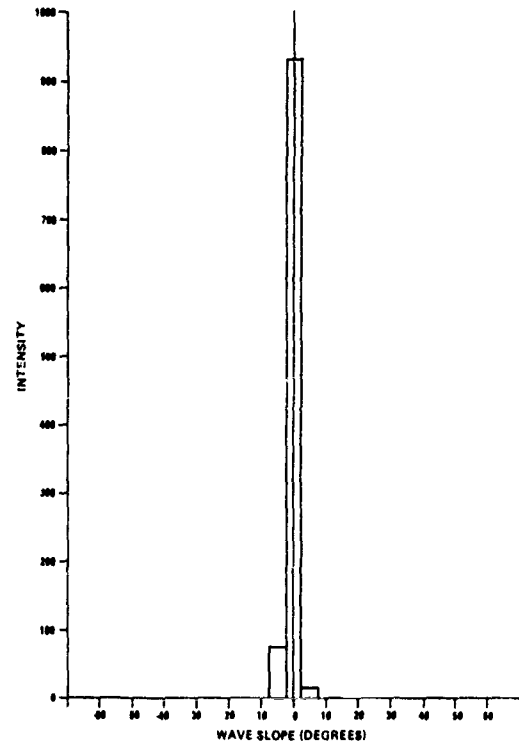


Figure 11. Wave Slope Distribution
for $W = 3.1$ m/sec

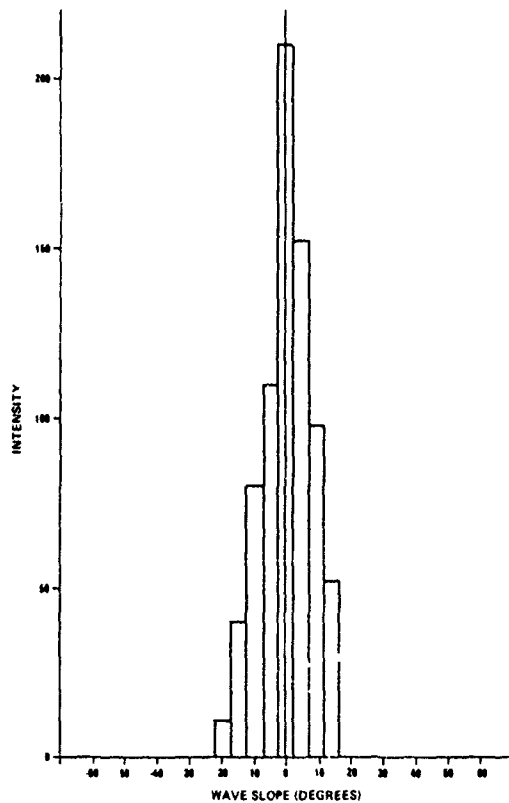


Figure 12. Wave Slope Distribution
for $W = 4.0$ m/sec

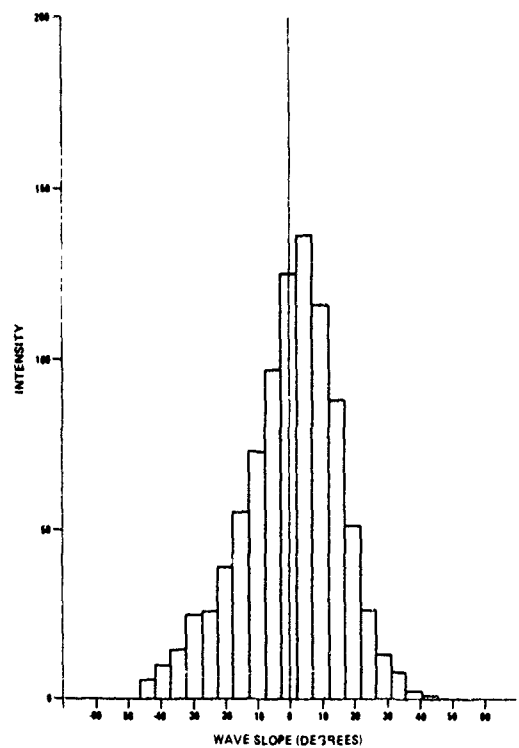


Figure 13. Wave Slope Distribution
for $W = 4.9$ m/sec

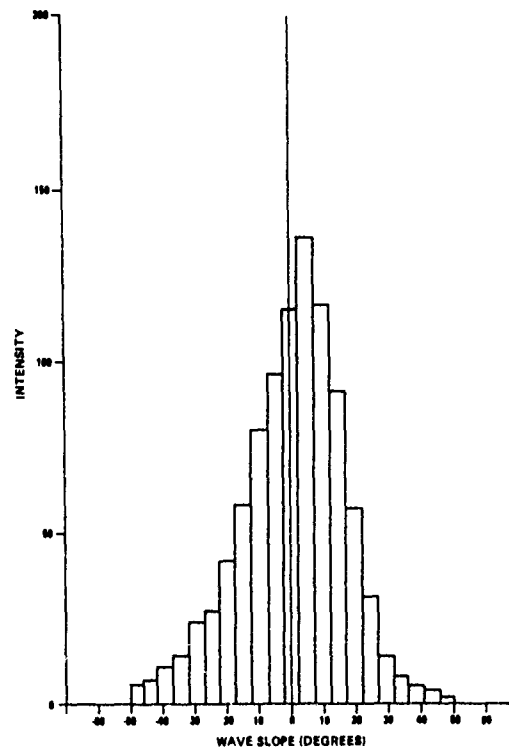


Figure 14. Wave Slope Distribution
for $W = 5.8$ m/sec

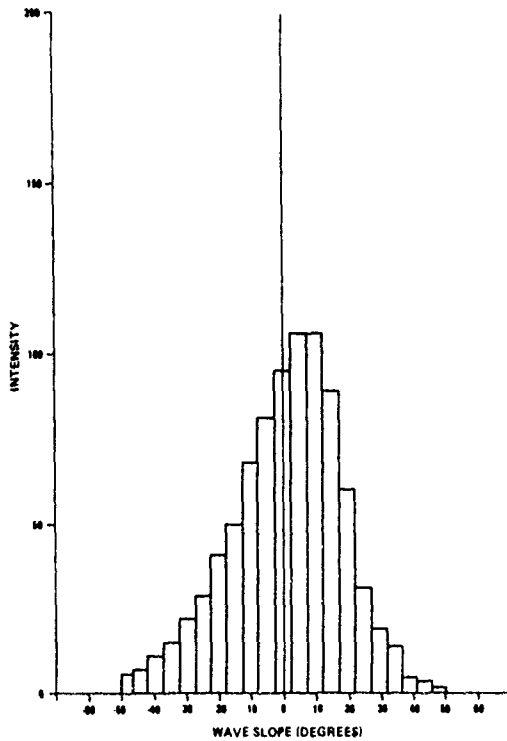


Figure 15. Wave Slope Distribution
for $W = 6.7$ m/sec

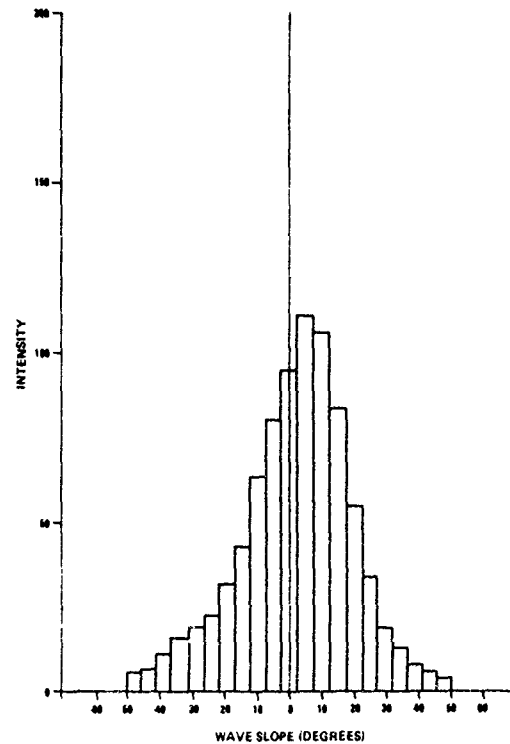


Figure 16. Wave Slope Distribution
for $W = 7.6$ m/sec

From the data in Figures 10 to 16, the rms wave slope may be calculated for each wind speed. A plot of this calculation is shown in Figure 17. The rms wave slope rises sharply with wind speed up to 5 meters per second, then begins to level off. If the steeply rising portion of the wave slope versus wind speed curve is extrapolated to zero, an onset velocity is found of $U_0 \sim 3$ meters per second. This value ($U_0 \sim 3$ meters per second) for the short fetch used in this study is quite compatible with the previous numbers given for the Cox study (Reference 6). In Figure 17 the data of Cox are plotted for a fetch of 1.47 meters for comparison. The values found in the present study for the rms wave slopes rise more steeply with wind speed and level off at a higher value. The ocean data of Cox and Munk (Reference 4) obtained from sunglint measurements are also shown in Figure 17. The ocean data differs from the wavetank data in two major respects: (1) there is no onset velocity in the 2 to 3 meters per second range, and (2) the rms values for the wave slopes at a given wind-speed are lower in the open ocean than in wavetanks. The smaller wave slopes in the open ocean have been attributed, at least in part, to the suppression of capillary wave growth by gravity waves (Reference 8).

In Figure 18 the full-angle beam divergence, which contains 50 percent of the energy of the beam, is plotted against wind speed for three different cases. The first case is represented by the four data points of Prettyman and Cermak (Reference 7) which show the beam divergence to be about 4 degrees and independent of wind speed. Their data was taken in the ocean using a laser source illuminating a submerged screen. The location of the laser spot (1/8-inch diameter) was filmed. The data from the present study are also plotted in Figure 18; the data points were obtained from Figures 10 through 16 by finding the full width of each histogram which contains half the power. The theoretical curve is calculated from a one-dimensional model using the value for the rms slope from the Cox and Munk study (Reference 4). There is a fair amount of

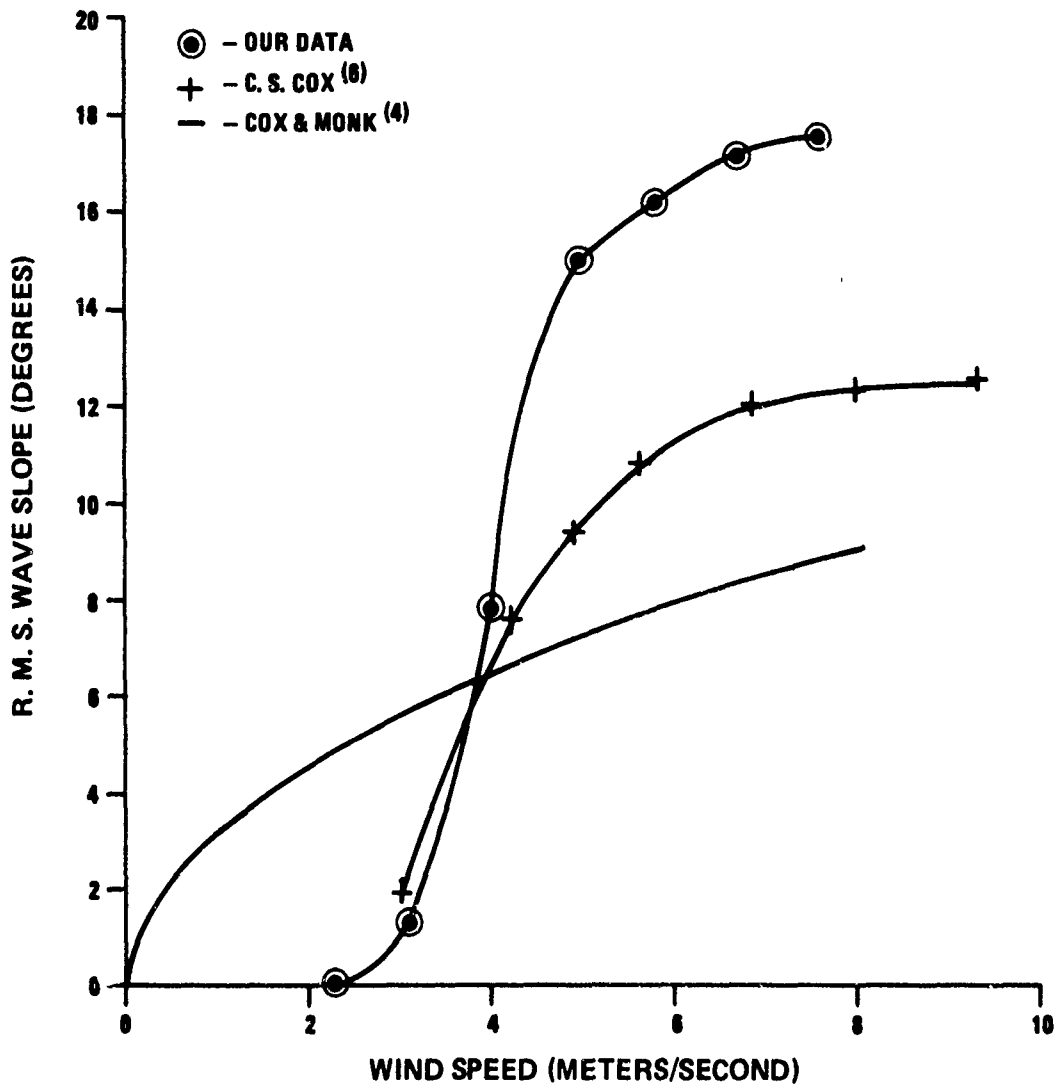


Figure 17. RMS Wave Slope Versus Wind Speed

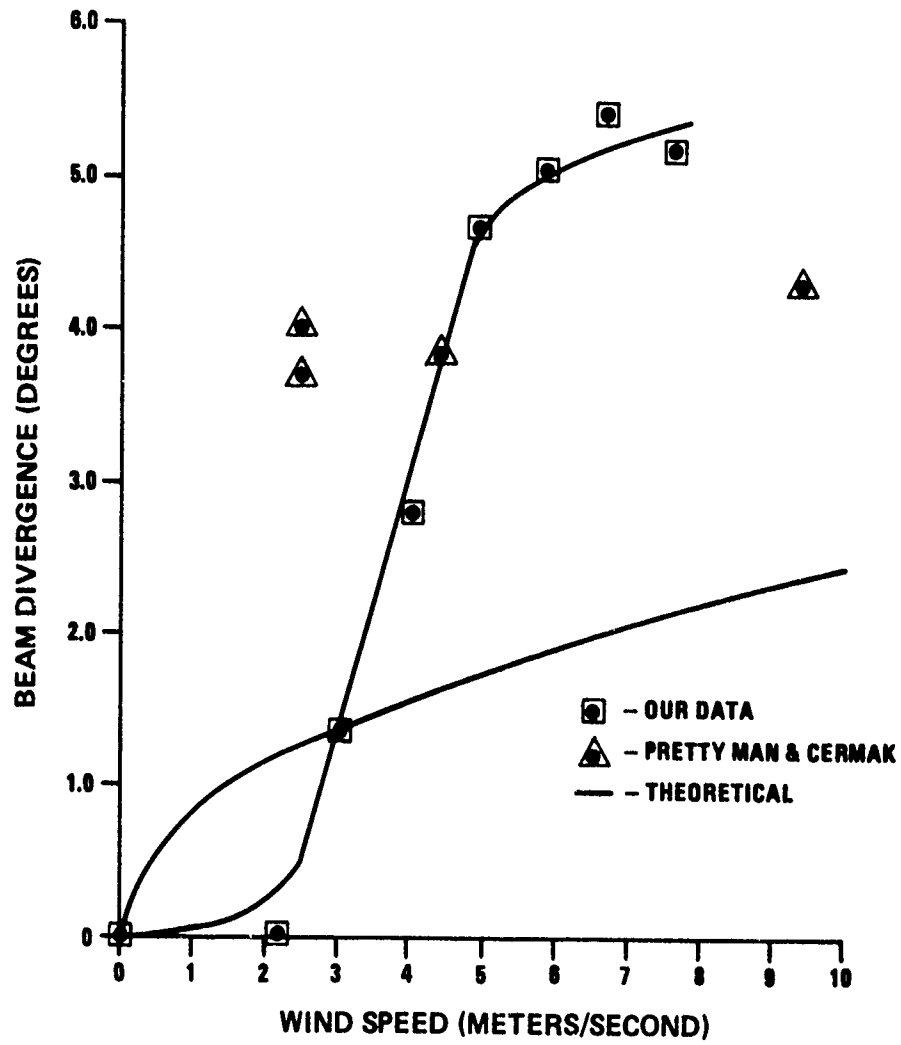


Figure 18. Beam Divergence Versus Wind Speed

discrepancy in the three results. The wavetank measurements of the present study are not expected to represent ocean conditions because of the short fetch and the absence of gravity waves. However, it is expected that there would be better agreement between the laser data of Prettyman and Cermak and the theoretical model which incorporates the Cox and Munk data. Also, a stronger dependence of laser divergence on wind speed is expected from the present study than is shown by the Prettyman and Cermak data.

One of the reasons for the lower rms wave slopes in the Cox and Munk paper could be related to the geometry of the capillary waves. In Figure 19 the capillary waveforms as calculated by Crapper (Reference 3) are shown for a/λ (amplitude/wavelength) values equal to 0.73, 0.53, and 0.34. When considering reflecting light from the $a/\lambda = 0.73$ capillary waves, it is found that adjacent waves obscure the higher slopes from being measured. For example, for the case $a/\lambda = 0.73$ and the elevation angle of the light source is 90 degrees (directly overhead), the highest measurable slope angle is approximately 40 degrees. If the above wave is assumed to be planar, then wave slopes greater than or equal to 40 degrees account for 34 percent of the reflection and refraction. This number is calculated by taking the horizontal projection of the wave envelope and measuring the fraction (F) of the projection for which the slope angle (σ) is greater than or equal to 40 degrees. For $a/\lambda = 0.73$, $F = 51$ percent for $\sigma \geq 30$ degrees. For $a/\lambda = 0.53$, $F = 39$ percent for $\sigma \geq 30$ degrees. And, for $a/\lambda = 0.34$, $F = 32$ percent for $\sigma \geq 30$ degrees. In this paragraph, extreme examples (high a/λ ratios) have been taken to make the point that the reflection technique systematically prevents the higher slope angles from being measured.

As seen in Figure 8, the mean capillary wave height for the highest wind speed (7.6 meters per second) is 8.8 millimeters; therefore, for capillary waves ($\lambda \leq 1.7$ centimeters) the ratio $a/\lambda \geq 0.52$. Consequently, a high percentage ($F \sim 39$ percent) of wave slopes greater than 30 degrees should be observed in Figure 16.

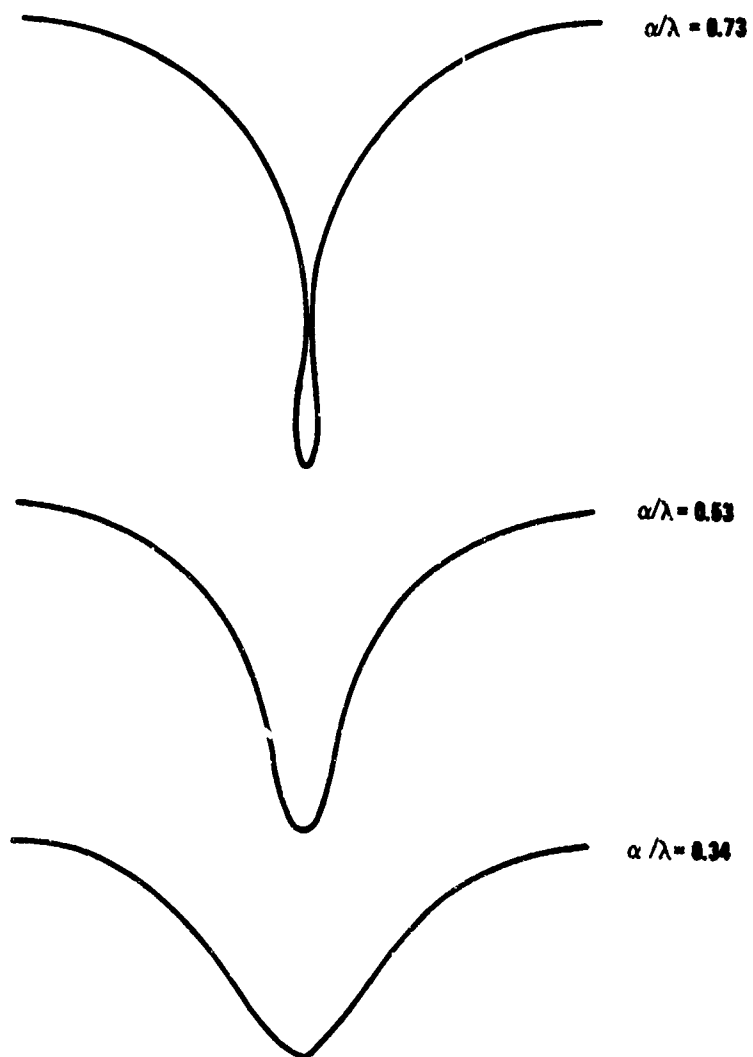


Figure 19. Capillary Wave Forms

However, the percentage measured from Figure 16 is $F \approx 8$ percent. This discrepancy could be due to impurities in the water used, the effects of wind on the wave shape, or applying a two-dimensional model to a three-dimensional world. In comparing these data to the model by Crapper (Reference 3), there is one last point worth making. The highest wave height measured in all of our data taking was 1.23 centimeters; if it is assumed that this wave height was associated with a capillary wave of maximum length (1.7 centimeters), then $a/\lambda = 0.72$. This value is in excellent agreement with the theoretical value ($a/\lambda = 0.73$) of Crapper.

SECTION 7

CONCLUSIONS

The following conclusions can be drawn from our study:

- a. The beam spreading due to the roughness of the air-sea interface is small compared with the spreading due to bulk scattering. Therefore, compensating for the interface would be of little benefit.
- b. Using a small-diameter laser beam substantially increases the irradiance on target for depths of 50 meters and less.
- c. The mean heights for capillary waves are in the range 0.06 to 8.8 millimeters for wind speeds 2.2 to 7.6 meters per second. These heights are consistent with theoretically allowed values for capillary waves.
- d. The spectral content of the wind-driven capillary waves is in the range 0 to 400 Hz with most of the intensity below 100 Hz. The high-frequency portions of the spectral curves grow at the expense of the low-frequency portions as the wind speed increases.
- e. The wavetank data on wave slopes yield higher values for full-width beam divergence (~ 5 degrees) than open-ocean data (~ 2 degrees and ~ 4 degrees) at wind speeds in the range of 5 to 8 meters per second.
- f. Fewer wave slopes of high angle are measured in these experiments than are predicted by theory.
- g. The onset wind velocity for wave generation is found to be ~ 3 meters per second.
- h. The shape of the wind-driven waves is affected by the wind.
- i. The wave height measurements furnish experimental support to the theoretical model of Crapper (Reference 3).

REFERENCE

1. C.B. Clark, Am. J. of Phys. 27, 478 (1959)
2. G. G. Stokes, Mathematical and Physical Papers, Volume 1, Cambridge University Press (1880).
3. G.D. Crapper, J. Fluid Mech. 2, 532 (1957).
4. C. Cox and W. Munk, J. Opt. Soc. Am. 44, 838 (1954).
5. D. Arnush, J. Opt. Soc. Am. 62, 1109 (1972).
6. C.S. Cox, J. Mar. Res. 16, 199 (1958).
7. C.E. Prettyman and M.D. Cermak, IEEE Geoscience Electronics GE-7, 235 (1969).
8. J. Wu., J. Geophys. Res. 82, 1359 (1977).

DISTRIBUTION LIST

REPORT NO. NADC-78253-30

NAVAIRDEVCON INDEPENDENT RESEARCH/ EXPLORATORY DEVELOPMENT PROGRAM

Work Unit No. GC181

	<u>No. of Copies</u>		<u>No. of Copies</u>
DARPA	1	DMA	1
(1 for Dr. P. Selwyn)		(1 for CDR Van Nield)	
U.S. Army, Ft. Monmouth, NJ	1	NOAA/NOS	1
(1 for Dr. R. Buser, DRSEL-LT-L)		(1 for Dr. G. Guenther)	
ARRADCOM	1	NOSC	3
(1 for K. Kramer, DRDAR-LCA)		(1 for Dr. E. Schimitchek)	
NAVPGSCOL	1	(1 for Dr. G. Mooradian)	
(1 for Library)		(1 for Technical Library)	
NAVAIRSYSCOM	2	APL/JHU	1
(1 for Dr. H.J. Mueller)		(1 for Dr. H. Heaton)	
(1 for B. L. Dillon)		Sylvania Electric	1
NAVOCERESDEVACT	1	(1 for Dr. P.J. Titterton)	
NAVELEX	1	Pacific Sierra Research Co.	1
(1 for L.W. Sumney)		(1 for Dr. R.F. Lutomirski)	
NCSC	1	UC San Diego	1
(1 for G. Gould)		(1 for Dr. S.Q. Duntley)	
NUSC, New London	1	Scripps Institute	2
(1 for Dr. W. Stachnik)		(1 for Dr. C.S. Cox)	
ONR, Boston	1	(1 for Dr. W. Munk)	
(1 for Dr. M. White)		IDA	1
ONR, Arlington	1	(1 for Dr. V.J. Corcoran)	
(1 for Dr. W.R. Condell)		SRI	1
NRL	3	(1 for Dr. R.C. Honey)	
(1 for Dr. J. McCallum)		DDC-TCA	12
(1 for Dr. S. Watt)			
(1 for Library)			

DISTRIBUTION LIST

REPORT NO. NADC-78253-30

NAVAIRDEVCON INDEPENDENT RESEARCH/ EXPLORATORY DEVELOPMENT PROGRAM

Work Unit No. GC181

	<u>No. of Copies</u>		<u>No. of Copies</u>
DARPA	1	DMA	1
(1 for Dr. P. Selwyn)		(1 for CDR Van Nield)	
U.S. Army, Ft. Monmouth, NJ	1	NOAA/NOS	1
(1 for Dr. R. Buser; DRSEL-LT-L)		(1 for Dr. G. Guenther)	
ARRADCOM	1	NOSC	3
(1 for K. Kramer, DRDAR-LCA)		(1 for Dr. E. Schimitchek)	
NAVPGSCOL	1	(1 for Dr. G. Mooradian)	
(1 for Library)		(1 for Technical Library)	
NAVAIRSYSCOM	2	APL/JHU	1
(1 for Dr. H.J. Mueller)		(1 for Dr. H. Heaton)	
(1 for B. L. Dillon)		Sylvania Electric	1
NAVOCERESDEVACT	1	(1 for Dr. P.J. Titterton)	
NAVELEX	1	Pacific Sierra Research Co.	1
(1 for L. W. Sumney)		(1 for Dr. R. F. Lutomirski)	
NCSC	1	UC San Diego	1
(1 for G. Gould)		(1 for Dr. S. Q. Duntley)	
NUSC, New London	1	Scripps Institute	2
(1 for Dr. W. Stachnik)		(1 for Dr. C.S. Cox)	
ONR, Boston	1	(1 for Dr. W. Munk)	
(1 for Dr. M. White)		IDA	1
ONR, Arlington	1	(1 for Dr. V.J. Corcoran)	
(1 for Dr. W.R. Condell)		SRI	1
NRL	3	(1 for Dr. R.C. Honey)	
(1 for Dr. J. McCallum)		DDC-TCA	12
(1 for Dr. S. Watt)			
(1 for Library)			